Korean J. Chem. Eng., 32(4), 617-628 (2015)
DOI: 10.1007/s11814-014-0241-x

pISSN: 0256-1115
eISSN: 1975-7220

Direct numerical simulations of inertial settling of non-Brownian particles

Ali Abbas Zaidi†, Takuya Tsuji, and Toshitsugu Tanaka

Department of Mechanical Engineering, Osaka University, Suita 565-0871, Japan
(*Received 12 March 2014 • accepted 20 August 2014*)

Abstract−The dynamics of particles settling at moderate Reynolds number is studied with periodic boundary conditions. The particle Reynolds number ranges from 0.1 to 50, and the solid volume fraction ranges from single sphere to 0.4. Particle-fluid interactions are solved by immersed boundary method and particle-particle interactions are solved by discrete element method. The principal results are the average settling velocity and the structure formation of particles. The average sedimentation velocities of particles for moderate Reynolds number showed deviation from the well-known power law, and the difference keeps on increasing with decrease in solid volume fractions. This deviation is removed by proposing the division of the power law into three regions of Reynolds number for dilute and non-dilute regimes. By analyzing the particle structures, this difference is due to the particle arrangements by the wake interactions at moderate Reynolds number.

Keywords: Hindered Settling Velocity, Sedimentation, Particle Structuring, Moderate Reynolds Number, Direct Numerical Simulation

INTRODUCTION

The transport properties of sedimenting particles play an important role in many natural and industrial processes and are fundamental phenomena in non-equilibrium suspension dynamics (non-Brownian and high Peclet number suspensions, where the Peclet number characterizes the strength of convection to that of diffusion). It uses gravitational force to separate particulate material from the fluid streams. Some of its specific applications are separating dirt and debris from incoming raw material, crystals from their mother liquor, dust or product particles from air streams and removal of contaminants in ground water. The understanding of sedimentation is challenging because of the long-range hydrodynamic interactions between particles and constantly changing suspension microstructure. There are reasonable numbers of investigations by experiments [1-3], theoretical analysis [4,5] and numerical simulations [6-12] to explain the physics of sedimentation for low Reynolds number. Moderate Reynolds number, i.e., when inertial effects of fluid become important, need careful attention of the numerical simulations. Thus we focused on particle settling for moderate range of Reynolds number, up to 50.

Different methods are available to simulate the particle settling such as Stokesian dynamics [10], Lattice Boltzmann method (LBM) [6,7], dissipative particle dynamics [13], stochastic rotation dynamics [8] (SRD) and immersed boundary method [14,15] (IBM). Further details of these methods can be found in Padding et al. [16] and Ladd et al. [7]. In the present study, we used body force type immersed boundary method (IBM) for simulations. The immersed boundary method uses a fixed Cartesian grid, and accounts for the fluid-particle interactions by introducing body force in the Navier-Stokes equation. Thus this approach enables us to reduce the computational time by the elimination of regeneration of grid at every time step with the movement of particles.

We propose a new relation for average settling velocity and to study the particle structures that are formed during sedimentation for the particle Reynolds number in the range of 0.1 to 50 and solid volume fraction from about single sphere to 0.4. The sequence which we will follow in this paper is: after introduction we will give a brief overview of formulation which we used in our simulations. It will be followed by simulation setup and testing of the factors which may affect the results; then we will present the results and describe the physics. Finally, we will conclude by key findings and acknowledgments.

NUMERICAL SCHEME

1. Immersed Boundary Method (IBM)

In the IBM by Kajishima et al. [17], which is used in the current simulations, the grid size is smaller than the size of the particles and the fluid flow is calculated by assuming the fluid occupies the entire domain, including the fluid and the particles. The effect of particles is expressed by a body force into the momentum equation of fluid, which constrains the no slip boundary condition at the particle surface. So the equations of continuity and incompressible Navier-Stokes equation are given by:

$$\nabla \cdot \mathbf{u}_f = 0 \tag{1}$$

$$\frac{\partial \mathbf{u}_f}{\partial t} + \mathbf{u}_f \cdot \nabla \mathbf{u}_f = \nu \nabla^2 \mathbf{u}_f - \frac{\nabla p}{\rho} + g \tag{2}$$

For the numerical integration, fluid-particle volume-weighted velocity is defined, which is given by:

$$\mathbf{u} = \alpha \mathbf{u}_p + (1-\alpha)\mathbf{u}_f \tag{3}$$

†To whom correspondence should be addressed.
E-mail: ali@cf.mech.eng.osaka-u.ac.jp

α takes the value zero for fluid and one for particle and in the range of zero to one at the interface. The velocity inside the solid particle is defined by:

$$\mathbf{u}_p = \nu_p + \omega_\mathbf{p} \times \mathbf{r} \tag{4}$$

For the case of no slip and no permeable conditions at the interface ($\mathbf{u}_f = \mathbf{u}_p$), the continuity restriction should also be satisfied for $\mathbf{u}$. The momentum equation of fluid in IBM is given by:

$$\frac{\partial \mathbf{u}}{\partial \mathrm{t}} + \mathbf{u}\cdot\nabla\mathbf{u} = \nu\nabla^2\mathbf{u} - \frac{\nabla \mathrm{p}}{\rho} + \mathbf{f}_p + \mathrm{g} \tag{5}$$

where $\mathbf{f}_p$ is the modification factor used to modify the flow predicted as if the field is occupied by fluid to the velocity defined by Eq. (3). The time-marching of Eq. (5) consists of two steps: in the first step the velocity is predicted by using Eq. (2) without taking into account of $\mathbf{f}_p$. For time marching of Eq. (2) the fractional step method based on Adams-Bashforth method of second-order accuracy in time is used.

$$\tilde{\mathbf{u}} = \mathbf{u}_{n0} + \frac{\Delta \mathrm{t}}{2}(3\mathbf{H}_{n0} - \mathbf{H}_{n0-1}) \tag{6}$$

$$\mathbf{H} = -\frac{\nabla \mathrm{p}}{\rho} - \mathbf{u}\cdot\nabla\mathbf{u} + \nu\nabla^2\mathbf{u} + \mathrm{g} \tag{7}$$

In the second step, the predicted velocity $\tilde{\mathbf{u}}$ is constrained to the volume-weighted velocity by the modification factor given by:

$$\mathbf{f}_p = \alpha(\mathbf{u}_p - \tilde{\mathbf{u}})/\Delta \mathrm{t} \tag{8}$$

The fluid force and fluid moment on a particle are calculated by the volume integral equations Eq. (9) and Eq. (10).

$$\mathbf{F}_f = -\rho\int_{\nu_p} \mathbf{f}_p \mathrm{d}\nu \tag{9}$$

$$\mathbf{M}_f = -\rho\int_{\nu_p} \mathbf{r}\times\mathbf{f}_p \mathrm{d}\nu \tag{10}$$

A general difficulty with IBM is its inability to resolve the fluid force when a pair of particles approach each other and the separation distance becomes comparable to or smaller than the grid spacing. This may affect the accuracy of results. To overcome this problem, rather than using fine mesh resolutions to resolve the flows in small gaps, we used the analytical results for the lubrication force to describe these short range interactions. The details of this method can be found Simeonov and Calantoni [18]. The lubrication force ($\mathbf{F}_\mathrm{l}$) between the two spheres which are going to collide diverges as the separation distance between the two spheres approaches zero. However, in real applications this divergence can be removed due to particle roughness and micro-asperities. To avoid singularity of the lubrication force Simeonov and Calantoni proposed that the lubrication force should be equal to zero if the ratio of inter-particle distance to particle diameter becomes less than the O (10^{-4}). In simulations the maximum distance at which the lubrication force is taken into account is when the surface to surface distance between particles becomes less than or equal to 1.5 grid points. However, if this distance is greater than one grid spacing, it has about negligible effect on the simulation results.

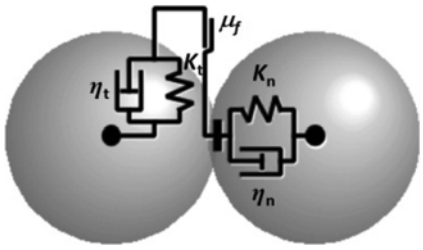

Fig. 1. DEM model.

2. Discrete Element Method

In DEM by Cundall and Strack [19] the contact force between two particles or particle and wall is modeled by springs, dashpots and friction slider.

$$\mathbf{F}_n = (-\mathrm{K}_n\delta_n - \eta_n\mathbf{G}\cdot\mathbf{n})\mathbf{n} \tag{11}$$

$$\mathbf{F}_t = (-\mathrm{K}_t\delta_t - \eta_t\mathrm{G}_{ct})\mathbf{t} \tag{12}$$

$$\text{If } |\mathbf{F}_t| > \mathrm{f}|\mathbf{F}_n| \tag{13}$$

$$\mathbf{F}_t = -\mathrm{f}|\mathbf{F}_n|\mathbf{t} \tag{14}$$

Besides fluid force, particle-particle interaction force and lubrication force, the gravitational force also acts on particles. It will be explained later that the gravitational force is used to control the settling Reynolds number.

3. Flow Chart of Formulation

Fig. 2 shows the algorithm of formulation.

All the forces on particles are calculated sequentially and then added-up at the end to calculate the velocity and displacement of particles. For time marching of velocities (Eqs. (15) and (16)) and displacements of particles (Eq. (17)), we have used second-order Adams-Bashforth and second-order Crank-Nicolson schemes, respectively.

$$\nu_p^{n0+1} = \nu_p^{n0} + \frac{\Delta \mathrm{t}}{2\mathrm{m}_p}(3(\mathbf{F}_f^{n0} + \mathbf{F}_{DEM}^{n0} + \mathbf{F}_l^{n0} + \mathbf{F}_g^{n0}) - (\mathbf{F}_f^{n0-1} + \mathbf{F}_{DEM}^{n0-1} + \mathbf{F}_l^{n0-1} + \mathbf{F}_g^{n0-1})) \tag{15}$$

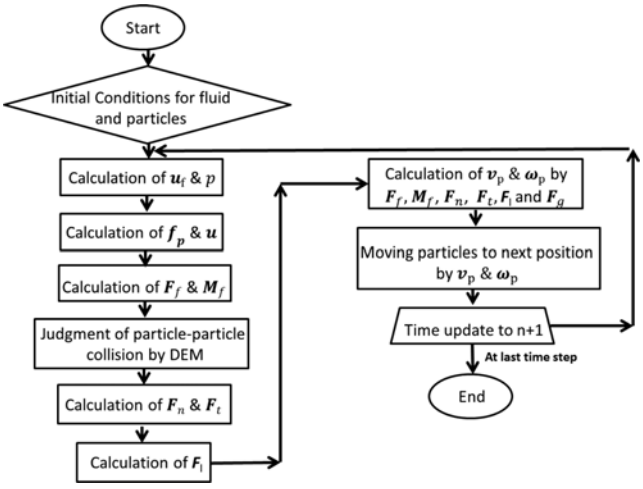

Fig. 2. Flow chart of formulation.

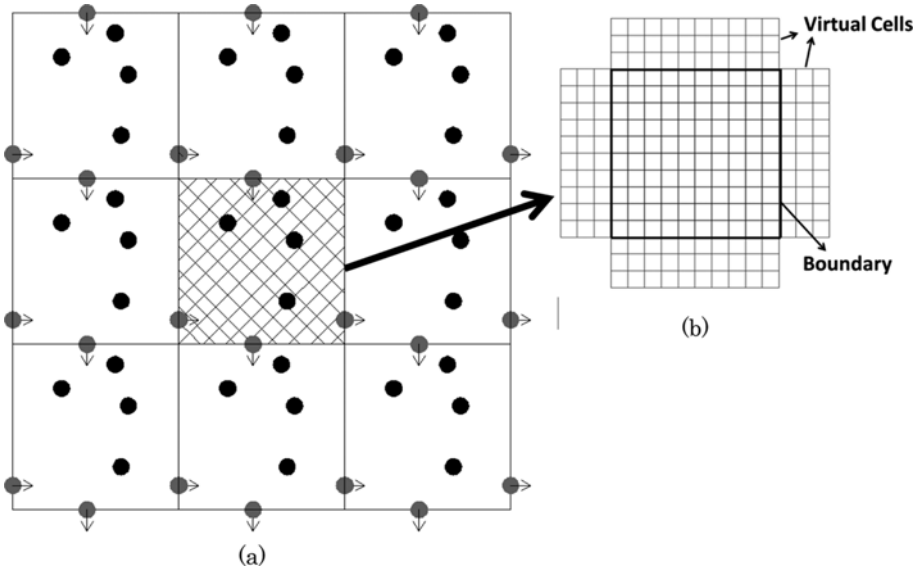

Fig. 3. Schematic of periodic boundary condition (a) Particles (b) fluid.

$$\omega_p^{n0+1} = \omega_p^{n0} + \frac{\Delta t}{2I_p}(3(\mathbf{M}_f^{n0} + \mathbf{M}_{DEM}^{n0} + \mathbf{M}_l^{n0}) - (\mathbf{M}_f^{n0-1} + \mathbf{M}_{DEM}^{n0-1} + \mathbf{M}_l^{n0-1})) \quad (16)$$

$$\chi_p^{n0+1} = \chi_p^{n0} + \frac{\Delta t}{2}(v_p^{n0+1} + v_p^{n0}) \quad (17)$$

SIMULATION SETUP

For the simulations we used the cubic computational domain of length L in each direction with periodic boundary condition and zero volume flow rate of fluid to mimic the unbounded suspension condition. Initially, the fluid is at rest and particles are randomly arranged by elastic collisions (in the absence of ambient fluid) of spheres from regular arrangements. The number of spheres in the domain is taken to obtain desired solid volume fraction. For explanation of periodic boundary condition, a two-dimensional schematic diagram is shown in Fig. 3.

The hatched area in Fig. 3(a) shows the actual computational domain. Periodic domain is usually used to replicate bigger domains without increasing the computational cost. When a particle leaves one face of a periodic boundary, it re-enters on the opposite face, thus keeping the solid volume fraction constant during calculations. In Fig. 3(a), grey particles indicate the particles leaving and re-entering the domain. For a fluid, the periodic boundary condition assumes that there are virtual cells or grid outside the boundary for both fluid pressure and velocity. The size of these virtual cells depends upon the space discretization. We used fourth-order central differencing; thus the size of these virtual cells is three grid points. Periodic boundaries of the opposite faces are connected, so any disturbance in fluid on one face of the boundary is propagated back in the computational domain from the opposite face.

Thus, during particle settling under the action of gravity, fluid efflux from the domain, also occurs in the gravity direction. If there is no external pressure gradient or volume flow rate applied to the fluid in the direction opposite to the fluid efflux, then the fluid will keep accelerating indefinitely. There are two possible ways to overcome this problem.

1. To apply a constant pressure gradient or constant volume flow rate opposite to fluid efflux.

2. To calculate the average fluid efflux from the domain at every time step and apply it as influx in the opposite direction to keep the volume flow rate in the computational domain to zero.

Method 2 gives better control over settling Reynolds number and is used in the present simulations. It was first used by Beetstra et al. [20] in the calculations of drag force on moving spheres for gas-solid flows in periodic boundary condition.

Three different initial particle distributions are studied for each case to get statistically reliable results. Furthermore, all the results presented in the next sections are time averaged for about 300-500 Stokes time ($t'=tU_s/d_p$). The fluid used in the simulations is water and the studied Reynolds number are Re≅0.1, 1, 10, 20, 30, 40 and 50 and solid volume fraction from single particle to 0.4. The particle Reynolds number is controlled by gravitational force on particles ($\mathbf{F}_g$) and is defined as:

$$\mathrm{Re} = \frac{U_s d_p}{\nu} \quad (18)$$

The following parameters are used for DEM solver:

We observed that the selection of parameters of DEM has negligible effect on the simulation results (since in liquid-solid systems the primary forces between particles are the hydrodynamic interactions). To reduce the computational time we used parallelized code by standard 1-D domain decomposition technique. For the

Table 1. DEM parameters [21]

Coefficient of restitution [-]	0.9
Normal spring constant [N/m]	800
Coefficient of particle friction [-]	0.25

Table 2. Test cases of domain sizes for different φ and Re

Re	φ	L/d_p
1	0.01	10, 25, 50
50	0.01	10, 25, 50
1	0.05	10, 20, 25
50	0.05	10, 20, 25
1	0.2	5, 10, 15
50	0.2	5, 10, 15

data transfers between CPUs, MPI library (MPICH2) is used.

1. Effect of Domain Size

For the effect of domain size we analyzed six cases of solid volume fractions and Reynolds number:

We observed that the averaged particle velocity showed more variation with increasing domain size for low solid volume fractions and low Reynolds number (e.g., in the case of Re=1 and φ= 0.01 the percentage difference from the largest domain size decreases from 10.8% to 3.1% for increasing L/d_p from 10 to 25 and in the case of Re=50 and φ=0.01 it decreases from 2.4% to 0.2% for increasing L/d_p=10 to 25). The reason for the comparatively larger variation observed in the cases of low solid volume fractions is the small number of particles to give statistically reliable results, and this tendency is more prominent for the case of low Reynolds number due to the long range hydrodynamic interactions. The domain size in the studied cases is selected in such a way that the percentage difference between two successive domain sizes which are used in analysing the effect of domain is less than 5%. For $\varphi \le 0.01$ and for $\varphi > 0.01$ we have taken L/d_p=25 and L/d_p=10 respectively.

2. Grid Resolution

Another important parameter in direct numerical simulation (DNS) is the number of grid points per particle diameter (d_p/dx). In suspensions where particles are free to move, two parameters are important for its selection, Re & φ. High Re and larger φ need fine grid resolution to resolve small scale fluid structures. We define $\varphi \le 0.1$ as dilute and $\varphi > 0.1$ as dense case. For low Reynolds number (Re≤1) and dilute case and low Reynolds number (Re≤1) and dense case ($\varphi > 0.1$) we observed that d_p/dx=8 and d_p/dx = 16 gives the grid converged results, respectively. For moderate Reynolds number we analyzed two test cases φ=0.05 and 0.4 as standard for dilute and dense cases for Re=50 (as it poses the greatest difficulty in the domain of parameters we studied). We calculated average particle velocity by increasing d_p/dx from 8 to 32 for φ=0.05 and 8 to 40 for φ=0.4 with increments of 8. For each d_p/dx the same initial particle distribution was used. For φ=0.05 the difference in the value of V_p for d_p/dx=6 and 32 is about 2.57% and for φ=0.4 the difference for d_p/dx=24 and 40 is 3.74%. Thus, we took d_p/dx=16 for dilute and d_p/dx=4 for dense cases for moderate range of Re. The variation of V_p with d_p/dx for moderate Reynolds number is shown in Fig. 4.

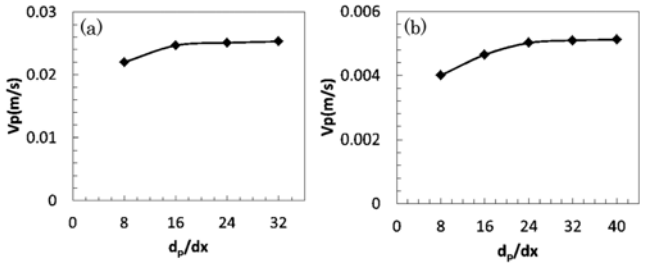

Fig. 4. Effect of d_p/dx on V_p (a) φ=0.05 and Re=50 (b) φ=0.4 and Re=50.

RESULTS AND DISCUSSION

1. Terminal Velocity

The settling or terminal velocity (U_s) of a single particle provides the simplest case for benchmarking of fluid-solver. Many literature data and mathematical relations are available for terminal velocity calculation. We used the relations of Hartman et al. [22] for the calculation of terminal Reynolds number (Re_∞) in an infinite medium.

$$\log_{10}Re_\infty = P + \log_{10}R \tag{19}$$

$$P = ((0.0017795C - 0.0573)C + 1.0315)C - 1.26222 \tag{20}$$

$$R = 0.99947 + 0.01853\sin(1.848C - 3.14) \tag{21}$$

$$C = \log Ar \tag{22}$$

$$Ar = \frac{\rho_f(\rho_p - \rho_f)g d_p^3}{\mu^2} \tag{23}$$

Table 3 compares the terminal velocity by simulation and the above relations.

The deviation between Eq. (19) and the simulation was observed to be less than 2.7% for all the cases. This calculated terminal velocity will be later used to normalize the hindered settling velocity in the next subsection; so that any of the finite size effects of the computational domain are minimized for hindered settling velocity calculation.

2. Hindered Settling Velocity

The mean settling velocity of uniform sized spheres is less than the terminal velocity of an isolated sphere due to the inter-particle interactions and this can be found in literature [e.g. work of Ham and Homsy [23], Al-Naafa and Selim [24]]. Experimentally, it is not easy to obtain the average particle settling velocity, especially for the dilute suspensions due to diffuse-clear fluid interface and spread in the particle size distribution (Davis and Birdsell [25]). Even for the measurement of particle terminal velocity uncertainty, up to 10% in the experimental results are possible (Di Felice [26]).

Table 3. Comparison of terminal velocity by simulation and Eq. (19)

Re	U_s by Eq. (19)	U_s by simulation	|Percentage Diff.|
1	0.00068	0.000683	0.4
10	0.0068	0.00671	1.3
20	0.013	0.0127	2.3
30	0.020	0.0195	2.5
40	0.0267	0.0261	2.2
50	0.033	0.0321	2.7

Thus numerical simulations give more reliable results by better control over the simulation setup and particle velocity calculations.

For comparisons, we have used the power law formula of Richardson and Zaki [27] (R&Z), based on their experimental results; which is widely used in chemical engineering applications. In this relation hindered settling velocity is expressed in terms of the terminal velocity of a single particle and void fraction. It is given by the following equation:

$$U = \frac{V_p}{U_s} = (1-\varphi)^{n_e} \tag{24}$$

where n_e is the power-law exponent, which depends on the terminal particle Reynolds number for moderate range of Reynolds number and constant for low and high Reynolds number. The equation of n_e proposed by R&Z is:

$$n_e = \begin{cases} 4.65 & Re < 0.2 \\ 4.4Re^{-0.03} & 0.2 < Re < 1 \\ 4.4Re^{-0.1} & 1 < Re < 500 \\ 2.4 & Re > 500 \end{cases} \tag{25}$$

Garside & Al-Dibouni (G&D) [28] proposed another equation of n_e by a single correlation:

$$\frac{5.1-n_e}{n_e-2.7} = 0.1Re^{0.9} \tag{26}$$

We show the comparison between the simulation data and the correlation by R&Z (Eq. (24) & (25)) in Fig. 5 and the percentage difference between them in Fig. 6.

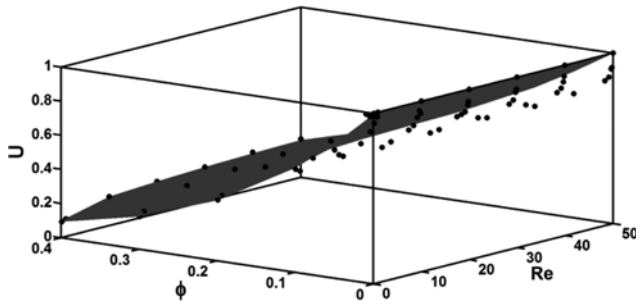

Fig. 5. Comparison of simulation data points (Black dots) and correlations of Eq. (24) & (25).

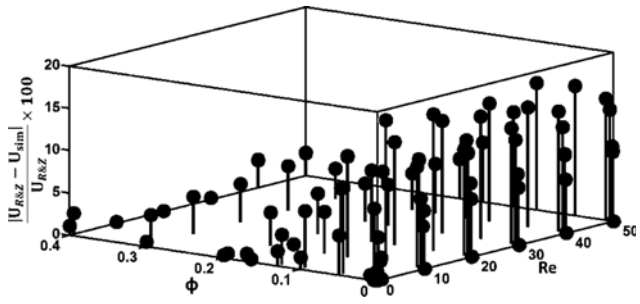

Fig. 6. Percentage difference of simulation data points and correlations of Eq. (24) & (25).

It can be observed that:

1. The R&Z relation reasonably agrees with the simulation data for low Reynolds number, Re≅0.1 and all studied φ. For Re>0.1, in very dilute ($\varphi \le 0.01$) and dilute regimes ($\varphi > 0.01$ and $\varphi \le 0.1$) the value of U by simulations is less than the prediction of R&Z, and the difference keeps increasing with the increase of Reynolds number (e.g., for φ=0.01 the percentage difference between the simulation data and R&Z correlation increases from 3.6% to 14.4% with increase of Re from 0.1 to 50). Moreover for $\varphi \le 0.01$ simulation results for U rapidly approaches the terminal velocity of single particle.

2. For dense case ($\varphi \ge 0.2$) the simulation results are in reasonable agreement with the R&Z correlation for all the range of studied Reynolds number (the max percentage difference between the simulation data and R&Z correlation in this range is 3.3% at Re=50).

The limits of Reynolds number proposed by R&Z are based on three different microstructures formed in sedimentation. These microstructures are different at different solid volume fractions, as will be explained in the next section, and thus affect the hindered settling velocity. Similar behavior of over-estimation of hindered settling velocity by R&Z was observed by the experiments of Di Felice [26] for dilute suspensions ($\varphi \le 0.05$) and Re=0.01-1000. Di Felice [26] suggested that this discrepancy can be removed by multiplying the right side of Eq. (24) by a multiplication factor k. He proposed that the value of k should be less than one.

$$U = k(1-\varphi)^{n_e} \tag{27}$$

We think that the exponent n_e to be the function of only Reynolds number is not sufficient to describe the averaged particle velocity at different solid volume fractions. We proposed that in the exponent besides Reynolds number there should also be a function of solid volume fraction for $\varphi > 0.01$ and a constant term for $\varphi \le 0.01$ to accommodate the changing structures during particle settling. Moreover, we also observed that the averaged particle velocity during settling for $\varphi \le 0.01$ and $\varphi > 0.01$ is quite different and difficult to express by a single relation. This may be due to the particle-particle hydrodynamic interactions, for $\varphi \le 0.01$ is different than for $\varphi >$ 0.01 because of fewer number of particles for $\varphi \le 0.01$. Thus, we propose the following relation for hindered settling velocity:

$$U = (1-\varphi)^{n_e} \tag{28}$$

if $\varphi \le 0.01$

$$n_e = \begin{cases} 4.65 & Re < 0.2 \\ 4.4Re^{-0.03} + 9.348 & 0.2 \le Re \le 1 \\ 4.4Re^{-0.1} + 15.74 & 1 < Re \le 50 \end{cases} \tag{29}$$

if $\varphi > 0.01$

$$n_e = \begin{cases} 4.65 & Re < 0.2 \\ 4.4Re^{-0.03} + 8.2(1-\varphi)^{26.33} & 0.2 \le Re \le 1 \\ 4.4Re^{-0.1} + 7.75(1-\varphi)^{16.81} & 1 < Re \le 50 \end{cases} \tag{30}$$

To visualize the effect of Eq. (28), Eq. (29) and Eq. (30), we have compared these equations with other relations and the simulation results in Fig. 7 for Re=0.1, 1, 20 and 50.

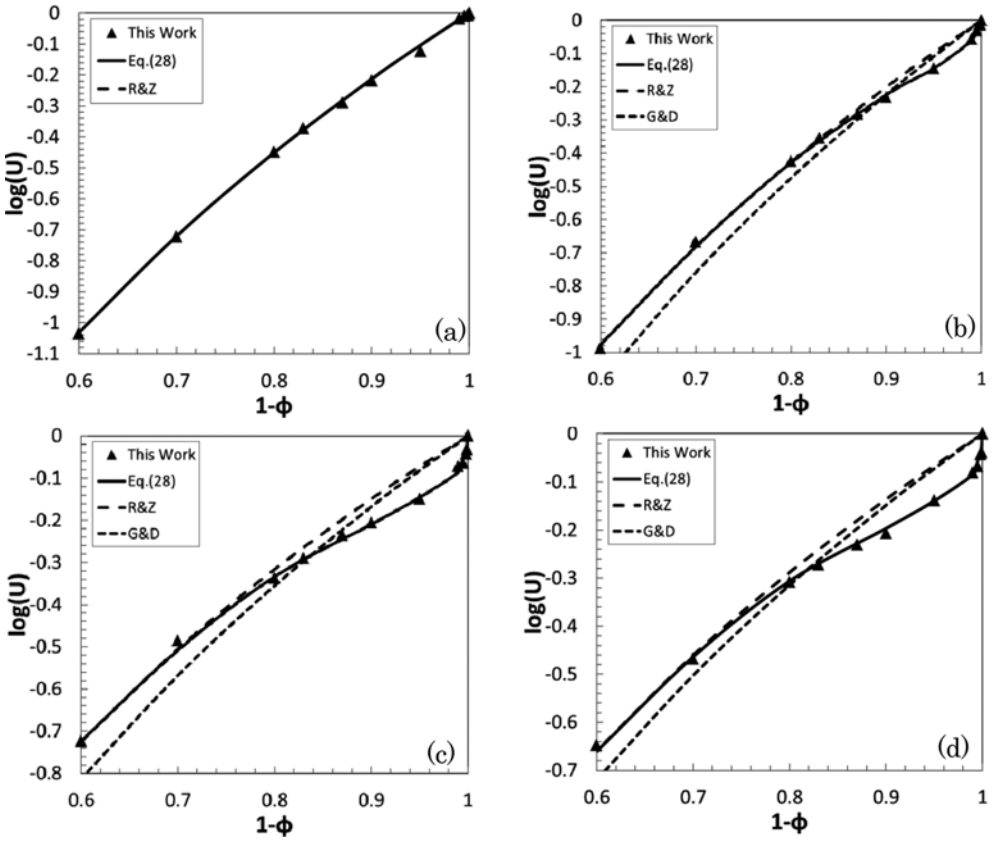

Fig. 7. Hindered Settling Velocity as function of (1−φ) Eq. (28) Eq. (29) Eq. (30) (a) Re=0.1 (b) Re=1 (c) Re=20 (d) Re=50.

Eq. (28), Eq. (29) and Eq. (30) give much better fit to the simulation data points in comparison with other relations in literature. Quantitatively, the percentage difference between this improved correlation and the simulation data is less than 3% for all Reynolds number. The mathematical relation of R&Z is based on their experiments on sedimentation and fluidization. In their experiments, most of the investigated cases for monodisperse spheres were greater than φ=0.06, and then they drew straight lines on log-log plots for settling velocity and void fraction. Thus, the discrepancy for low solid volume fractions could not be found clearly by R&Z. Since we carefully used the simulation parameters and analyzed a reasonable number of discrete data (both for φ and Re) for proposing the relation for average settling velocity, we believe that the Eq. (28), Eq. (29) and Eq. (30) are reliable and accurate.

We also calculated the value of k from Eq. (27) and found that k is a function of Reynolds number for $0.01 \le \varphi \le 0.1$. We drew the trend line of k for $\varphi \le 0.1$, which can be expressed by the following equation:

$$k = 0.1 Re^{-0.3} + 0.82 \quad (31)$$

For φ>0.2 the value of k fluctuates between 0.95-1.05. Although we only performed simulations up to Re=50, from the trend of variation of k in Fig. 8 it can be seen that the variation of k with Reynolds number after Re≥10 is slow and saturates after Re=40. Based on the experiments of Di Felice [26] (who suggested the value of k between 0.8-0.9) and intuition, we think that our proposed relation for averaged particle velocity can be valid for the range of

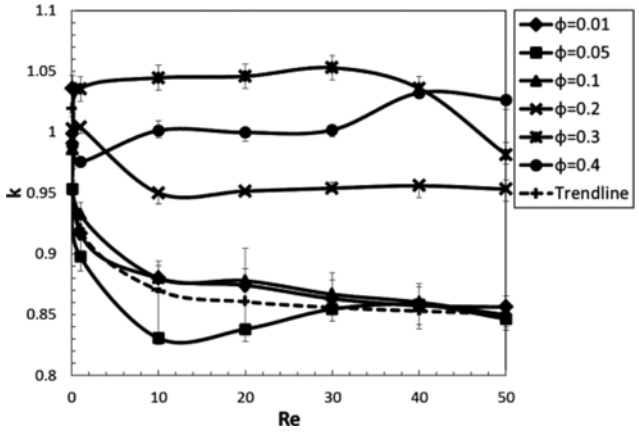

Fig. 8. Variation of k with Reynolds number.

Reynolds number in which the wakes around the particles are similar as in the cases we studied. Wakes around the particles in the range of studied Reynolds number are axisymmetric and attached ring type. It is proposed that such wakes remain possible up to Re≅ 210 [29]. After, the vortex ring becomes non-axisymmetric (about Re≅210-270) and finally into unsteady vortex shedding regime (Re≅ 300). In the unsteady vortex shedding regime the particles cluster due to trapping of particles in the wakes, and thus U becomes greater than one for low solid volume fractions [29-31].

Adhering to the statement that Eq. (28), Eq. (29) and Eq. (30)

are reliable and accurate for the studied ranges of φ and Re, we admit that the proposed mathematical model is obtained by curve fitting. The mathematical relation for settling velocity for dilute suspension and viscous flow regime can be obtained theoretically [32]. However, when inertial effects are no longer negligible (about Re> 1) and in the case of dense suspensions the integration of Navier-Stokes equations is not possible. To the extent of our knowledge of settling velocity relations in inertial flow regime [26-28], curve-fitting is used in the model development. However, in curve-fitting the simulation data and model development, care is taken to remain consistent with the form of the established mathematical model of literature. The new model only includes the necessary modification, i.e., addition of terms in n_e for Re>0.2.

3. Structure Formation in Suspension

Two particles in stokes flow condition fall with weak wake interactions and give rise to the long range velocity perturbations [8,9]. However, for moderate Reynolds number, the symmetrical fore and aft flow structure across the particle breaks and the wakes from the leading particle affect the downstream particle, thus leading to drafting kissing and tumbling scenario [33] (DKT). In the case of more than two particles, these interactions become much more complex and anisotropic. Thus, the structures of particles should be non-random. These particle structures are difficult to study experimentally, and that's why in literature the experimental work [34-36] is primarily focused on two dimensions and low solid volume fractions.

In DNS, it is possible to keep track of a reasonable number of particles accurately for long durations. For the analysis of particle structure formation under the effect of different solid volume fraction and Reynolds number, we studied particle clusters (which are local group of particles with large correlations), radial distribution function (RDF) and pair distribution function.

3-1. Cluster Analysis

A cluster is defined as a group of particles such that each particle is within a distance ad_p of another particle in the cluster. Particles which do not have a neighbor particle within ad_p are not considered in the same cluster. We used the method proposed by Herrmann et al. [36] for percolation problem, i.e., two particles of diameter d_{pi} and d_{pj} with positions $\mathbf{r}_i$ and $\mathbf{r}_j$ are considered to be in the same cluster if

$$|r_i - r_j| \le \frac{a(d_{pi} + d_{pj})}{2} \tag{32}$$

As we took mono-disperse spheres so both d_{pi} and d_{pj} are d_p. The parameter 'a' is critical in cluster size classification. The domain size and the solid volume fractions can give some idea for its selection but still it is not explicit. Wylie and Koch [37] proposed that this parameter should be larger than the lubrication cut-off distance (they took a lubrication cut-off distance equal to $0.01d_p$) and smaller than the particle radius to keep the qualitative trend of particle clusters similar. Xiong et al. [38] studied this parameter and observed that their results remain qualitatively the same by changing it from 1.05 d_p to 1.2 d_p. We analyzed this parameter for φ=0.05 and Re=50 and analyzed the fraction of particles participating in cluster of any size for different values of a. We observed that for a≤1.25 the temporal evolution patterns were almost not affected. We took a=1.05

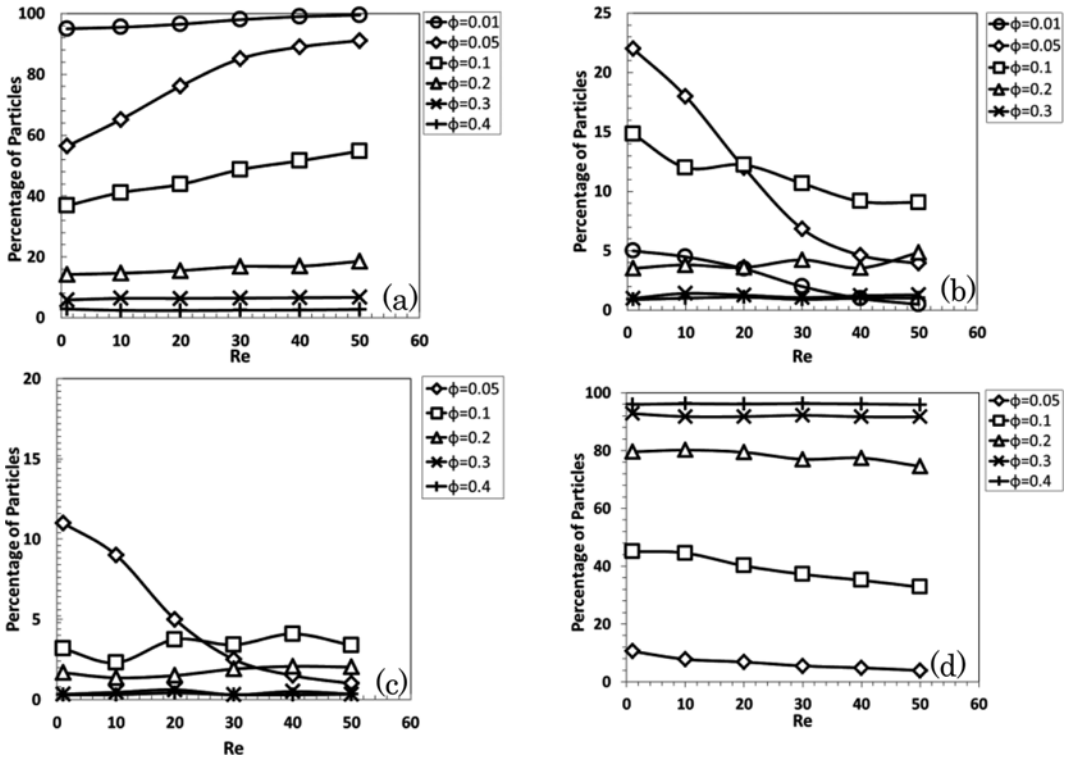

Fig. 9. Percentage of particles participating in clusters of (a) Single particle size, (b) Two particle size, (c) Three particle size, (d) More than three particle size.

throughout our simulations because it worked well for all studied solid volume fractions.

After the steady state was established we calculated the fraction of particles as single particles, two particle clusters (doublets), three particle clusters (triplets) and clusters of more than three particles, and time averaged the results for about 300 stokes time after the steady state. The results are shown in Fig. 9. For φ=0.01 the particles only formed doublets so we only show them till two particle clusters in the plots.

From Fig. 9, for the same Reynolds number the particle clustering increases with the increase in solid hold up. This is indicated by the decrease in the fraction of single particles as the solids hold up increases from 0.01 to 0.4. This is consistent with the statistical intuition: as the solid volume fraction increases, the average inter-particle distance decreases and hence more particles move collectively.

The Reynolds number adversely affects the degree of particle clustering and this effect is more evident for low solid volume fractions. For example for φ=0.01 and Re=50 about all of the particles are not participating in any cluster, and for φ=0.05 the fraction of particles that are not participating in any clusters increases from about 0.56 to 0.91 for increase of Reynolds number from 1 to 50. The effect of Reynolds number becomes less as the solid volume fraction increases and we observe almost no effect for φ=0.3 & 0.4.

One more point that we would like to discuss in this section is the effect of domain size on particle clustering. For Re≤1 and $\varphi\leq$ 0.01, the percentage of single particles decreased (i.e. from about 99% to 95% for L/d_p from 10 to 50), or in other words, particle clustering increased with the domain size. However, for Re>1 and $\varphi\leq$0.01 or φ>0.01 and all studied range of Reynolds number, domain size negligibly affected the particle clustering. Thus, the conclusion of this section, i.e. particle clustering is inversely proportional to the Reynolds number for dilute suspension and about independent with Reynolds number for dense suspension is still valid for larger domain sizes.

3-2. Radial Distribution Function (RDF)

Another measure of the suspension microstructure is the radial distribution function (RDF). It is usually plotted as a function of the inter-particle distances and gives us the information about overall structures formed in the suspension. Some of its features are that its value is always zero for distances less than particle diameter as particles cannot approach more closer than particle diameter, the appearance of peaks in the value of RDF indicates a higher probability of finding particles and at very long range RDF tends to a value of 1, which happens because RDF describes the average number density at this range. RDF g(r) is defined by the equation:

$$g(r)=\frac{n(r)}{4\pi\rho^{n}r^{2}\Delta r} \tag{33}$$

This function is averaged over all particles to give information for the overall structure. Furthermore, the RDF's shown in the Fig. 10 are time averaged for about 300 Stokes time after steady state. For comparison with the RDF for hard spheres (HS) we calculated the RDF for the Percus-Yevick equation [39,40] and shown in Fig. 10.

For dense cases (φ=0.2) there is no significant effect of Reynolds number on RDF, and it is quite similar like hard sphere distributions for all the Reynolds number. However, for a relatively dilute case (φ=0.05), the particle distribution in settling is different from the random distribution of spheres. For Re=0.1-1 the particles show more close pairs with higher peaks of RDF at smaller shell radius in comparison with random particles. However, as the Reynolds number increases for Re>1, RDF changes both in magnitude of the peak value and the region where this peak lies (the peak value shifts to r/d_p=2 and the peak value changes from 1.35 to 1.18 for Re=30-50). However at long inter-particle distances, i.e., $r/d_p\geq$3, the particle distributions show randomness with RDF≅1. The reason for the decrease in the particle clustering and the behavior of RDF with Reynolds number will be explained in the next section.

3-3. Pair Distribution Function

RDF gives information of the probability of particles in a shell, regardless of their position. For anisotropic suspensions like particles settling under gravity, it is necessary to investigate whether the particles prefer some particular directions. To study the orientation preferences of settling particles, the pair distribution function in cylindrical coordinates is calculated. Pair distribution function is

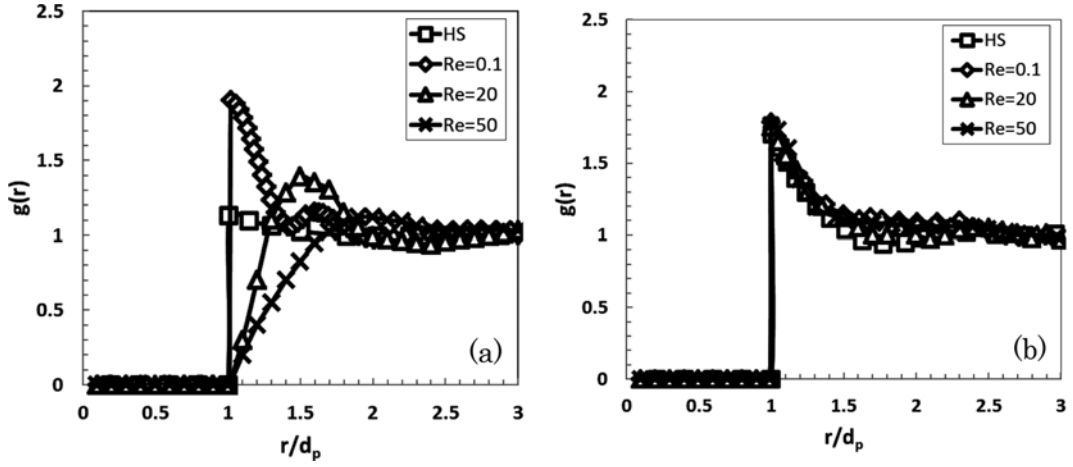

Fig. 10. Radial distribution function for (a) φ=0.05 (b) φ=0.2.

defined as:

$$g_1(r)=\frac{2L^3}{n_p^3}\langle\sum_{i<j}\delta(r_1-r_{1_{ij}})\rangle \quad (34)$$

The angled brackets show ensemble averaging. The pair distribution function in cylindrical coordinates $g_1(r_{cyd}, y)$ is averaged over θ where θ and r_{cycl} is given by.

$$\theta=\tan^{-1}\frac{z}{x} \quad (35)$$

$$r_{cycl}=\sqrt{x^2+z^2} \quad (36)$$

y is the height in the settling direction. $g_1(r)$ for φ=0.05 and φ=0.2 is shown in Fig. 11 as an example. The dotted lines are drawn at $0.5d_p$, $1d_p$, $1.5d_p$, $2d_p$ and $2.5d_p$ and the inside black circles show the particle surface.

The plot of pair distribution function for φ=0.05 shows anisotropy of suspension. The particles prefer horizontal positions with respect to the neighboring particles. Furthermore, this anisotropy increases with the increase in Reynolds number. For φ=0.2, the effect of Reynolds number diminishes and the particles obtain more isotropic structures.

Physics of microstructures and hindered settling during particle settling

For explaining the physics we divide the problem into three cases:

Case 1: Low solid volume fraction ($\varphi\leq$0.1) and low Reynolds number (Re≤1)

Case 2: Low solid volume fraction ($\varphi\leq$0.1) and moderate Reynolds number (Re>1)

Case 3: High solid volume fraction (φ>0.1) and low and moderate Reynolds number.

For case 1, the flow around the particles remains attached to the sphere. Because of the hydrodynamic interactions between particles, the particles form pairs, but because of the presence of very weak wakes they remain in contact for longer times and remain stable in the form of particle pairs. We think that the behavior of near particle pairs and high peaks of RDF at r/d_p=1 for Case 1 in Figure 10 is due to this weak wake interactions. Similar phenomenon was also observed in the simulations of Hamid et al. [41] and Brady et al. [42] in their investigations of the effects of hydrodynamic forces on non-Brownian settling particles.

For case 2, as the Reynolds number increases from the Stokes condition, fluid inertia breaks the attached flow around the particles and downstream wakes are generated. These wakes from the leading particles reduce the drag for the trailing particle. The trailing particle therefore approaches the leading particle. Koch [43] proposed if the particle inertia is small, then the trailing sphere drifts away from the wake of the leading particle under the effect of Saffman lift force rather than touching the leading particle. However, if the particle inertia is large the two spheres come into contact with each other, and then the trailing sphere rotate and the particles form horizontal pairs. This horizontal arrangement of particles is unstable and makes the particles move away from each other into pairs at some separation distance perpendicular to the settling

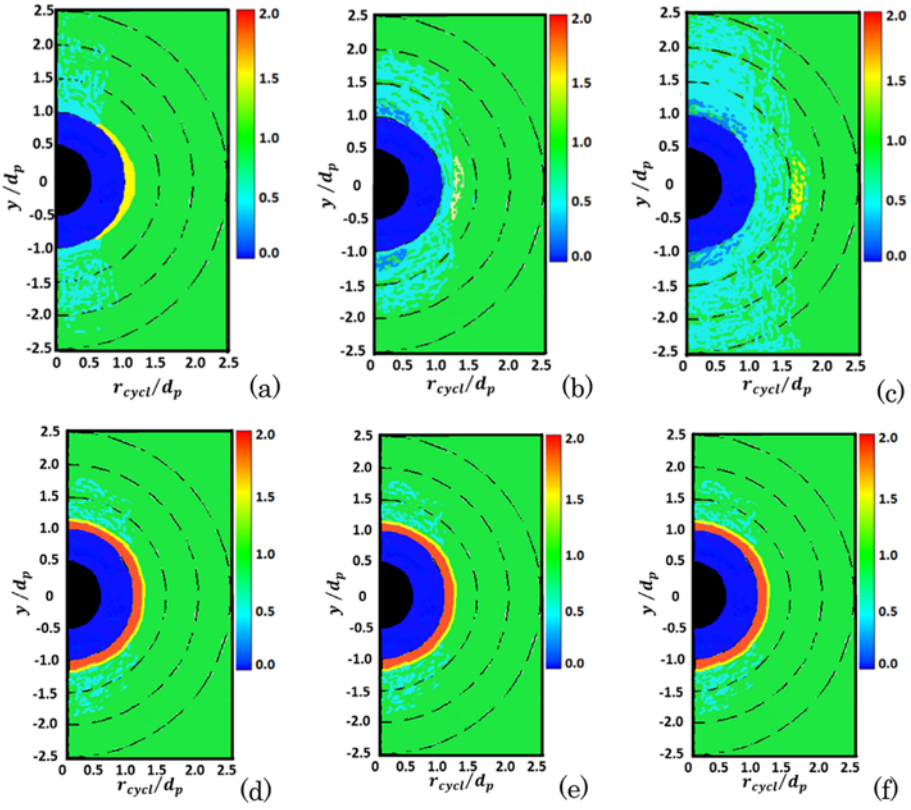

Fig. 11. Pair distribution function for (a) φ=0.05, Re=0.1 (b) φ=0.05, Re=20 (c) φ=0.05, Re=50 (d) φ=0.2, Re=0.1 (e) φ=0.2, Re=20 (f) φ=0.2, Re=50.

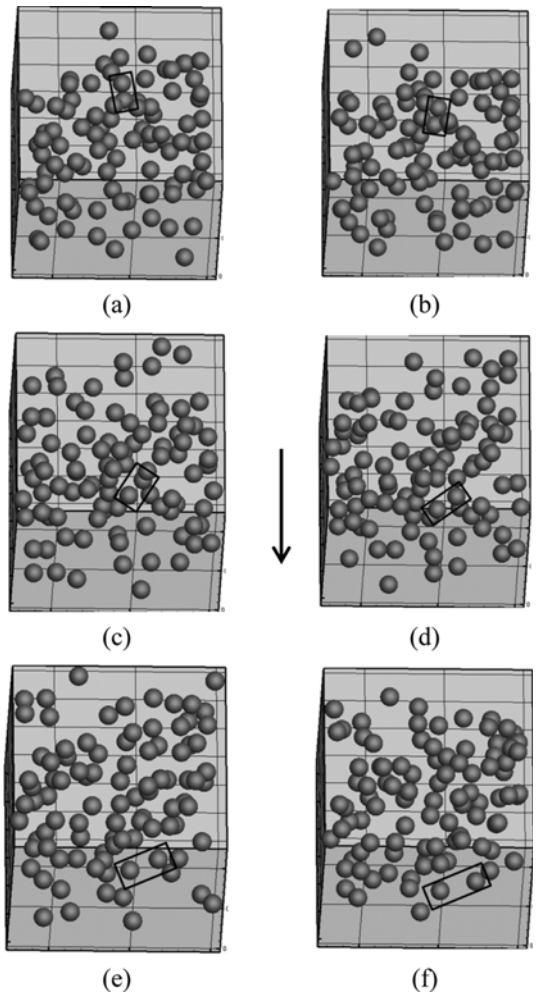

Fig. 12. Sequential snapshots of Drafting-Kissing and Tumbling (DKT) event observed in the present simulation (φ=0.05, Re=50) (Arrow shows gravity direction).

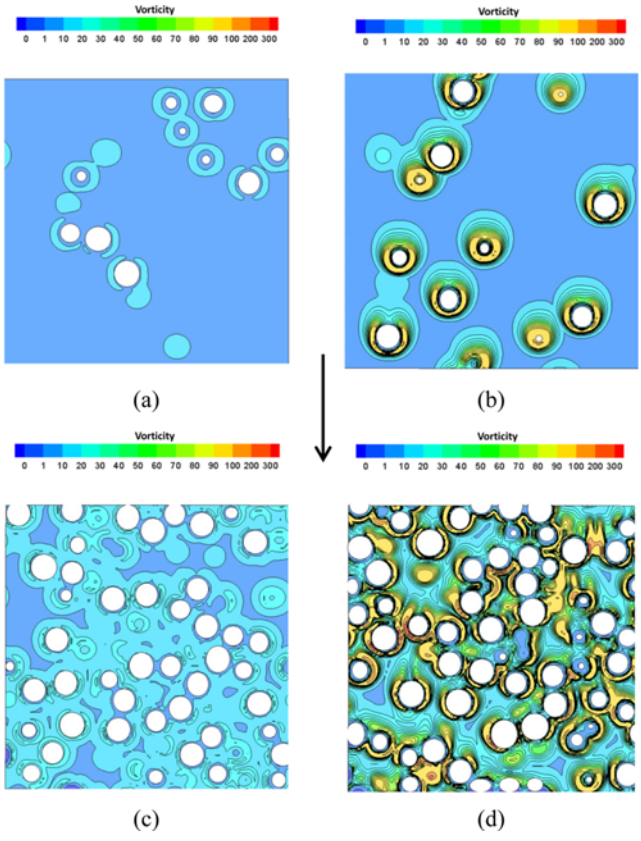

Fig. 13. Contour plot of vorticity (a) φ=0.05 & Re=1 (b) φ=0.05 & Re=50 (c) φ=0.3 & Re=1 (d) φ=0.3 & Re=50 (Arrow shows gravity direction).

direction. This phenomenon is called drafting, kissing and tumbling [33] (DKT). After DKT the particles remain separated as the particles experience repulsion fluid force in side-by-side arrangements. In the case of low φ, there is comparatively larger space for particles to move, so the DKT events can occur more easily. This leads to separated particles perpendicular to the gravity direction as observed in pair distribution function and decrease in the magnitude of RDF for smaller shells.

For case 3 because of the smaller inter-particle distances the hindered settling effect dominates the other effects mentioned for the other two cases. This leads to relatively isotropic particle structures (as can be seen in pair distribution function) similar to the distribution of hard sphere molecules, as was observed in the RDF, and makes the particle distribution independent of the Reynolds number.

A sequential snapshots of one of the DKT events observed in the simulation for φ=0.05 and Re=50 is shown in Fig. 12. In this case the particles have sufficient inertia that enables the particles to kiss rather than drift-out from the wakes during the drafting stage.

To see the interactions of wakes between particles, distributions of magnitude of vorticity in the computational domain are shown in Fig. 13. Fig. 13 shows the contour plots of the slice at the middle of the computational domain for φ=0.05 and 0.3 and Re=1 and 50. In the figure the white circles are the particle cross-sections.

As the Reynolds number increases, the intensity and area of vorticity region around the particles also increases, and thus the downstream wakes affect a greater region. On the other hand, when the solid volume fraction increases the wake structures are perturbed among many particles because of small inter-particle spacing.

The deviation of average particle velocity from the power law of Richardson and Zaki was only observed for case 2. This can be due to the particle microstructures which are developed from the DKT events. As already mentioned, the DKT events will lead to horizontally separated particles and thus the drag force experienced by each particle will be increased because of absence of particle motions in the wakes of other particles for longer times. Thus, this reduces the average particle velocity of spheres in comparison with the power law associated with the random sphere distributions.

CONCLUSIONS

The dynamics of settling particles is numerically predicted in the cubic domain with periodic boundaries by using immersed boundary method and discrete element method. The Reynolds number based on the terminal velocity of particles ranges from 0.1 to 50, and the solid volume fraction ranges from single sphere to 0.4. The

settling velocity for low solid volume fractions and moderate Reynolds number deviates from the established power law of Richardson and Zaki. Such a deviation is observed in the region of $0.002<\varphi<0.1$. By observing the particles' settling behavior, this deviation is due to the particle structures formed by the DKT events during settling. By using the present simulation data, we proposed a mathematical relation for the hindered settling velocity. We observed that the Reynolds number has an adverse effect on particle pairing and clustering as observed by analyzing particle clusters and the radial distribution function. For high solid volume fractions, because of the smaller inter-particle distance, the effects of the Reynolds number on the spatial structure of particles diminish.

ACKNOWLEDGEMENTS

We would like to acknowledge the Ministry of Education, Culture, Sports, Science & Technology, Japan for providing financial assistance. We are also grateful to Cybermedia Center, Osaka University and Center for Computing & Media Studies, Kyoto University for providing computational resources.

NOMENCLATURE

$\mathbf{u}_f$: fluid velocity [m-s^{-1}]
p : fluid pressure [N-m^{-2}]
t : time [s]
$\mathbf{u}$: fluid particle volume weighted velocity [m-s^{-1}]
$\mathbf{u}_p$: velocity inside the particle [m-s^{-1}]
v_p : velocity of particle center [m-s^{-1}]
ω_p : angular velocity of particle [s^{-1}]
r : unit vector from the center of rotation to the surface [m]
$\mathbf{f}_p$: modification factor [m-s^{-2}]
$\tilde{\mathbf{u}}$: predicted velocity [m-s^{-1}]
Δt : time step [s]
$\mathbf{F}_f$: fluid force [N]
$\mathbf{M}_f$: fluid moment [N-m]
V_p : volume of cube, whose sides enclose all the interfacial cells [m^3]
$\mathbf{F}_n$: normal contact force on particle [N]
$\mathbf{F}_t$: tangential contact force on particle [N]
K : spring constant [N-m^{-1}]
f : friction coefficient
$\mathbf{G}$: relative particle velocity between particles during collision [m-s^{-1}]
$\mathbf{n}$: normal unit vector at the contact point
$\mathbf{t}$: tangential unit vector at the contact point
$\mathbf{F}_{DEM}$: force acting on particle due to particle-particle collision [N]
$\mathbf{F}_l$: lubrication force acting on particle [N]
$\mathbf{F}_g$: gravitation force acting on particle [N]
$\mathbf{M}_{DEM}$: moment acting on particle due to particle-particle collision [N-m]
$\mathbf{M}_l$: moment acting on particle due to lubrication force [N-m]
m_p : mass of particle [kg]
I_p : moment of inertia [kg -s^{-2}]
x_p : particle displacement [m]
L : length of the side of cubic computational domain [m]
t′ : stokes time
U_s : terminal velocity of single particle [m-s^{-1}]
d_p : particle diameter [m]
Re : Reynolds number
dx : grid size [m]
V_p : average particle velocity [m-s^{-1}]
Re_∞ : terminal Reynolds number
Ar : archimedes number
g : gravity [m-s^{-2}]
n_e : power-law exponent
k : multiplication factor
a : parameter used for cluster classification
g(r) : radial distribution function
n(r) : number of particles in the shell of radius r
Δr : shell radius [m]
$g_1(r)$: pair distribution function
n_p : number of particles
r_1 : position vector between center of particles
θ : angular cylindrical coordinate
x, y, z : inter-particle length in x, y and z Cartesian directions [m]

Greek Letters

ρ : density [kg-m^{-3}]
ν : kinematic viscosity [m^2-s^{-1}]
α : volume fraction of particles at a targeted cell
δ : particle overlap during collision [m]
η : damping coefficient
φ : solid volume fraction
μ : viscosity [N-s-m^{-2}]
ρ^n : number density [m^{-3}]

Subscripts and Superscripts

n0 : previous time step
n : normal direction
t : tangential direction
f : fluid
p : particle

REFERENCES

1. H. Nicolai and E. Guazzelli, *Phys. Fluids*, **7**, 3 (1995).
2. H. Nicolai, B. Herzhaft, E. J. Hinch, L. Oger and E. Guazzelli, *Phys. Fluids*, **7**, 12 (1995).
3. H. Nicolai, Y. Peysson and E. Guazzelli, *Phys. Fluids*, **8**, 855 (1996).
4. R. E. Caflisch and J. H. C. Luke, *Phys. Fluids*, **28**, 759 (1985).
5. M. P. Brenner, *Phys. Fluids*, **11**, 754 (1999).
6. N. Q. Nguyen and A. J. C. Ladd, *J. Fluid Mech.*, **525**, 73 (2005).
7. A. J. C. Ladd and R. Verberg, *J. Stat. Phys.*, **104**, 1191 (2001).
8. J. T. Padding and A. A. Louis, *Phys. Rev. Lett.*, **93**, 220601 (2004).
9. J. T. Padding and A. A. Louis, *Phys. Rev. E*, **74**, 031402 (2006).
10. J. W. Swan and J. F. Brady, *Phys. Fluids*, **19**, 113306 (2007).
11. S. Koo, *Korean J. Chem. Eng.*, **28**, 364 (2011).
12. D. Nishiura, A. Shimosaka, Y. Shirakawa and J. Hidaka, *Proc. Chem. Eng.*, **32**, 331 (2006).
13. P. J. Hoogerbrugge and J. M. V. A. Koelman, *Europhys. Lett.*, **19**, 5 (1992).

14. F. R. Cunha, G. C. Abade, A. J. Sousa and E. J. Hinch, *J. Fluid Eng-T ASME*, **124**, 957 (2002).
15. J. M. Stockie, *Comp. Structures*, **87**, 701 (2009).
16. J. T. Padding and A. A. Louis, *Phys. Rev. E*, **77**, 011402 (2008).
17. T. Kajishima, S. Takiguchi, H. Hamasaki and Y. Miyake, *JSME Int. J. B-Fluid T*, **44**, 526 (2001).
18. J. A. Simeonov and J. Calantoni, *Int. J. Multiphase Flow*, **46**, 38 (2012).
19. P. A. Cundall and O. D. L. Strack, *Geotechnique*, **29**, 47 (1979).
20. R. Beetstra, M. A. Van der Hoef and J. A. M. Kuipers, *AIChE J.*, **53**, 489 (2007).
21. Y. Tsuji, T. Kawaguchi and T. Tanaka, *Powder Technol.*, **77**, 79 (1993).
22. M. Hartman, D. Trnka and V. Havlin, *Chem. Eng. Sci.*, **47**, 3162 (1992).
23. J. M. Ham and G. M. Homsy, *Int. J. Multiphase Flow*, **14**, 533 (1988).
24. M. A. Alnaafa and M. S. Selim, *AIChE J.*, **38**, 1618 (1992).
25. R. H. Davis and K. H. Birdsell, *AIChE J.*, **34**, 123 (1988).
26. R. Di Felice, *Int. J. Multiphase Flow*, **25**, 559 (1999).
27. J. F. Richardson and W. N. Zaki, *Trans. Inst. Chem. Eng.*, **32**, S82 (1954).
28. J. Garside and M. R. Aldibouni, *Ind. Eng. Chem. Proc. Dd.*, **16**, 206 (1977).
29. T. Kajishima, *Int. J. Heat Fluid Flow*, **25**, 721 (2004).
30. T. Kajishima and S. Takiguchi, *Int. J. Heat Fluid Flow*, **23**, 639 (2002).
31. T. Doychev and M. Uhlmann, Proc. of the 8th Int. Conf. on Multiphase Flow, May 2013, 320.
32. G. K. Batchelor, *J. Fluid Mech.*, **52**, 245 (1972)**.**
33. A. F. Fortes, D. D. Joseph and T. S. Lundgren, *J. Fluid Mech.*, **177**, 467 (1987).
34. Y. M. Chen, C. S. Jang, P. Cai and L. S. Fan, *Chem. Eng. Sci.*, **46**, 2253 (1991).
35. L. Talini, J. Leblond and F. Feuillebois, *J. Magn. Reson.*, **132**, 287 (1998).
36. H. J. Herrmann, D. C. Hong and H. E. Stanley, *J. Phys. A*, **17**, L261 (1984).
37. J. J. Wylie and D. L. Koch, *Phys. Fluids*, **12**, 964 (2000).
38. Q. G. Xiong, B. Li, F. G. Chen, J. S. Ma, W. Ge and J. H. Li, *Chem. Eng. Sci.*, **65**, 5356 (2010).
39. E. Thiele, *J. Chem. Phys.*, **39**, 474 (1963).
40. M. S. Wertheim, *Phys. Rev. Lett.*, **10**, 321 (1963).
41. A. Hamid and R. Yamamoto, *Phys. Rev. E*, **87**, 022310 (2013).
42. G. Bossis and J. F. Brady, *J. Chem. Phys.*, **87**, 5437 (1987).
43. D. L. Koch, *Phys. Fluids A*, **5**, 1141 (1993).